

The thermal structure and mechanical behavior of the martian lithosphere



Alberto Jiménez-Díaz ^{a,b,*}, Isabel Egea-Gonzalez ^c, Laura M. Parro ^d, Miki Tasaka ^e, Javier Ruiz ^d

^a Departamento de Biología y Geología, Física y Química Inorgánica, ESCET, Universidad Rey Juan Carlos, 28933 Móstoles, Madrid, Spain

^b Instituto de Ciencias de la Tierra Jaume Almera, ICTJA, CSIC, 08028 Barcelona, Spain

^c Departamento de Física Aplicada, Escuela Superior de Ingeniería, Universidad de Cádiz, 11519 Puerto Real, Cádiz, Spain

^d Departamento de Geodinámica, Estratigrafía y Paleontología, Facultad de Ciencias Geológicas, Universidad Complutense de Madrid, 28040 Madrid, Spain

^e Department of Geoscience, Interdisciplinary Graduate School of Science and Engineering, Shimane University, 1060 Nishikawatsu-cho, Matsue-shi, Shimane 690-8504, Japan

ARTICLE INFO

Keywords:

Geophysics

Mars

Mars, interior

Terrestrial planets

ABSTRACT

In depth knowledge of the thermal and rheological properties of the crust and mantle of Mars is fundamental for constraining the strength of its lithosphere, and thereby for the understanding its geodynamics, tectonics, and thermal evolution. In this context, an interesting debate on Martian crustal composition is ongoing. The presence of highly differentiated rocks at several locations, and their implications for the thermal state, structure, and evolution of the planet are not well understood. Here we systematically explore the effects of crust material properties (specifically thermal conductivity and density) on the thermal and mechanical structure of the Martian lithosphere. For this purpose, we analyze different key indicators of the thermal state, the strength and mechanical behavior of the lithosphere under a wide range of conditions. We do so by considering suitable parameters for both a nominally basaltic Martian crust and an end-member basaltic crust that would include a significant low density and high thermal conductivity component. We find that crust material properties have a strong control over the thermal state of the entire lithosphere, and thereby over the strength of the lithospheric mantle. Although a lower crustal density reduces the brittle strength, the colder geotherm due to a higher thermal conductivity leads to a stronger crust and lithospheric mantle, and therefore to a thicker lithosphere. It also leads to a stronger lithosphere as a whole in terms of total strength and effective elastic thickness, as a consequence of higher crust and mantle contributions. On the other hand, we also investigate the influence of the rheology of Mars' upper mantle on the total strength of its lithosphere. Water content has a large effect on the rheology of the upper mantle. A wet rheology implies a substantial reduction of the mantle contribution to the total strength and effective elastic thickness of the lithosphere, resulting in a significantly weaker lithosphere as a whole. Our results will serve both to improve our understanding of geophysical observations from the InSight and ExoMars missions, and to further constrain theoretical modeling efforts.

1. Introduction

In depth knowledge of the thermal and rheological properties of the crust and uppermost mantle (together forming the lithosphere) is fundamental for deciphering and understanding the thermal state, interior dynamics, and evolution of a planetary body. Indeed, the lithosphere is the outer rigid layer of solid-surface planets, and its behavior is a key factor controlling global geodynamics, heat transfer between the deep planetary interior and surface, and potentially the existence and nature of seismicity (for a review see Watters and Schultz, 2010; Arte-mieva, 2011; Turcotte and Schubert, 2014). Currently, our knowledge of

the properties of the Martian lithosphere come from indirect methods, which usually are proxies for lithospheric strength—mainly the effective elastic thickness of the lithosphere (e.g., Solomon and Head, 1990; McGovern et al., 2002; Grott et al., 2005; Ruiz et al., 2006a, 2011) or from depth to the brittle–ductile transition (BDT) beneath large thrust faults (e.g., Schultz and Watters, 2001; Grott et al., 2007; Ruiz et al., 2008, 2009; Mueller et al., 2014; Egea-González et al., 2017; Herrero-Gil et al., 2019). Also, based on the relationship between the thermal state of lithospheric rocks and their mechanical strength, these lithospheric strength proxies can be used to reconstruct the temperature distribution pattern, and to calculate the heat flow lost by Mars in the analyzed

* Corresponding author at: Departamento de Biología y Geología, Física y Química Inorgánica, ESCET, Universidad Rey Juan Carlos, 28933 Móstoles, Madrid, Spain.

E-mail address: alberto.jimenez.diaz@urjc.es (A. Jiménez-Díaz).

regions. The so-obtained heat flows are valid for the time when the lithosphere was loaded or faulted, and therefore—when deduced from regions deformed in different time periods—provides information on the thermal evolution of Mars (Ruiz et al., 2011; Ruiz, 2014).

Our current knowledge of the present-day lithosphere of Mars comes mostly from studying the loading of the lithosphere of the polar regions by the northern and southern polar ice caps. The flexural response of the lithosphere to the weight of the polar caps has allowed scientists to estimate their respective effective elastic thicknesses (Phillips et al., 2008; Wieczorek, 2008), and hence to derive calculations of the present-day surface heat flow (Ruiz et al., 2010, 2011; Parro et al., 2017), because lithospheric loading by the polar caps is a recent event (Laskar et al., 2002; Phillips et al., 2008). On the other hand, Sori and Bramson (2019) recently estimated the present-day, local heat flow necessary to generate the proposed melting of ice at the base of the south polar layered deposits (Orosei et al., 2018). The InSight mission (Banerdt and Russell, 2017) is now providing direct geophysical measurements at its landing site at Elysium Planitia (Golombek et al., 2017, 2018). These measurements will include seismological (Lognonné et al., 2019) and heat flow (Spohn et al., 2018) data, which will contribute to a substantial improvement of our knowledge and understanding of the Martian lithosphere, having implications for the whole planet. Thus, placing the InSight results (together with the deductions based on lithospheric strength and thermal indicators at the polar regions) into a wider geo-dynamic context must be an important objective for Martian science. Moreover, the ExoMars 2020 mission will also provide useful information toward a better understanding of the thermal state of Mars from data acquired—most likely in Oxia Planum.

Crustal composition must be taken into account when dealing with modeling the thermal and mechanical nature of the lithosphere of Mars, because different kinds of rocks have different thermo-mechanical properties. The composition of the Martian crust has been usually considered to be mostly basaltic. However, some recent works suggest that the Martian crust could contain a substantial amount of highly differentiated, silica- and feldspar-rich rocks, located in the southern hemisphere of Mars (Carter and Poulet, 2013; Wray et al., 2013; Baratoux et al., 2014; Sautter et al., 2015; Morris et al., 2016), although other works consider non-solids to the reason for orbital-based evidence for a felsic component (see Rogers and Nekvasil, 2015). Otherwise, Baratoux et al. (2014) proposed a high density for the Martian basalts, although these authors recognize that a crust so dense seems incompatible with geophysical studies, possibly favoring the presence of a felsic component.

Finally, Zhao et al. (2009) have reported that anhydrous olivine crystal aggregates are considerably weaker when they are proportionally iron-rich, precisely as expected for the Martian mantle (see also Kohlstedt and Mackwell, 2010), which would largely reduce its strength. Likewise, recent careful examinations of the creep behavior of olivine (the main mineral in the lithospheric mantle) aggregates under hydrous conditions as a function of iron content, suggest that the viscosity of the Martian mantle will be a factor of ~5–20 lower than the viscosity of Earth's mantle (Tasaka et al., 2015; Zhao et al., 2018).

All of these issues motivate us to explore the present-day thermal and mechanical structure of the lithosphere of Mars for a wide range of heat flow scenarios—by taking into account the proposed felsic component of the Martian crust for the purposes of comparison, and the possible influence of recent creep behavior laws for olivine aggregates under Martian conditions. This will provide us an integrated overview of the role of the crust and lithospheric mantle within the framework of the thermal and mechanical structure of the lithosphere of Mars, and will serve both to improve our understanding of geophysical observations of Mars and to further constrain theoretical modeling efforts.

In the following sections, we first describe the methodology, data, and parameters that are implemented for this study. We then carefully and systematically explore the effects of crustal density and thermal conductivity on the thermal structure and rheology of the lithosphere as

a function of surface heat flow and crustal thickness; in this way we identify the parameters that have a major impact on the thermal state and mechanical behavior of the lithosphere. We consider a nominal model (Model 1), which is characterized using reasonable parameters for a basaltic crust equivalent to that usually used for a global geophysical investigation of Mars (Zuber et al., 2000; Neumann et al., 2004; Genova et al., 2016). Because crustal density and thermal conductivity could be affected by the composition of the crust (specifically, the presence of a substantial felsic component, which would reduce density and increase thermal conductivity), it is important to evaluate their potential mechanical effects. Thus, we also consider a second model (Model 2). Finally, we also explore the effect of rheology of the mantle lithosphere for total lithospheric strength (Model 3), and we discuss the implications of our results for the present-day thermal state and structure of Mars.

2. Thermal state of the lithosphere: methods

The thermal structure of any lithosphere depends on its heat flow, distribution of lithospheric heat-producing elements (HPEs), and the thermal conductivity of lithospheric rocks. Following the procedure described by Ruiz et al. (2011), temperature profiles in the crust are calculated by assuming a homogeneous distribution of radioactive heat sources (see below). Furthermore, we use a constant thermal conductivity for the entire crust, and therefore the temperature at a given depth z is given by

$$T_z = T_{z0} + \frac{F_s z}{k_c} - \frac{\rho_c H_c z^2}{2 k_c}, \quad (1)$$

where T_{z0} is the surface temperature, F_s is the surface heat flow, k_c is the thermal conductivity of the crust, ρ_c is the density of the crust, and H_c is the crustal heat production rate per unit mass. We use a surface temperature of 220 K, the present-day mean surface temperature on Mars (Kieffer et al., 1977). Model 1, which corresponds to the nominally basaltic Martian crust, assumes a crustal density of 2900 kg m^{-3} , suitable for a basaltic crust (e.g., Zuber et al., 2000; McGovern et al., 2002; Ruiz et al., 2008), and a thermal conductivity of $2 \text{ W m}^{-1} \text{ K}^{-1}$, a value appropriate for basaltic rocks (this value is in the uppermost part of the range for intact, non-porous, basalts; see the compilation by Beardmore and Cull, 2001). Model 2 assumes a crustal density of 2750 kg m^{-3} and a thermal conductivity of $2.5 \text{ W m}^{-1} \text{ K}^{-1}$, which are more appropriate for felsic material (Fountain et al., 1990; Beardmore and Cull, 2001); this is an extreme way to consider the effect of a felsic component on a basaltic crust.

The significant homogeneity of elemental abundances measure by Mars Odyssey GRS suggests that the Martian crust is much less geochemically diverse than the Earth's crust (Taylor et al., 2006), which is consistent with strong mixing as a result of impact cratering (Taylor et al., 2006), and with the absence of large-scale crustal recycling, at least since the early part of the history of Mars (Frey, 2006). Thus, we assume crustal potassium and thorium abundances (3652 and 0.69 ppm, respectively), based on K and Th surface average values measured by Mars Odyssey GRS (Hahn et al., 2011), whereas U abundance is determined by assuming a Th/U ratio of 3.8 (e.g., Meyer, 2003; Hahn et al., 2011), which correspond to a present-day average heat production of $4.86 \times 10^{-11} \text{ W kg}^{-1}$.

The thermal conductivity of olivine (the main mineral in lithospheric mantle rocks) is strongly temperature-dependent, and therefore we calculate temperature profiles in the mantle lithosphere using

$$\frac{dT}{dz} = \frac{F_m - \rho_m H_m(z - T_c)}{k_m(T)}, \quad (2)$$

where $F_m = F_s - \rho_c H_c T_c$ is the mantle heat flow (i.e., the heat flow at the base of the crust), ρ_m and H_m are, respectively, the density and heat production rate per mass unity of the lithospheric mantle, T_c is the

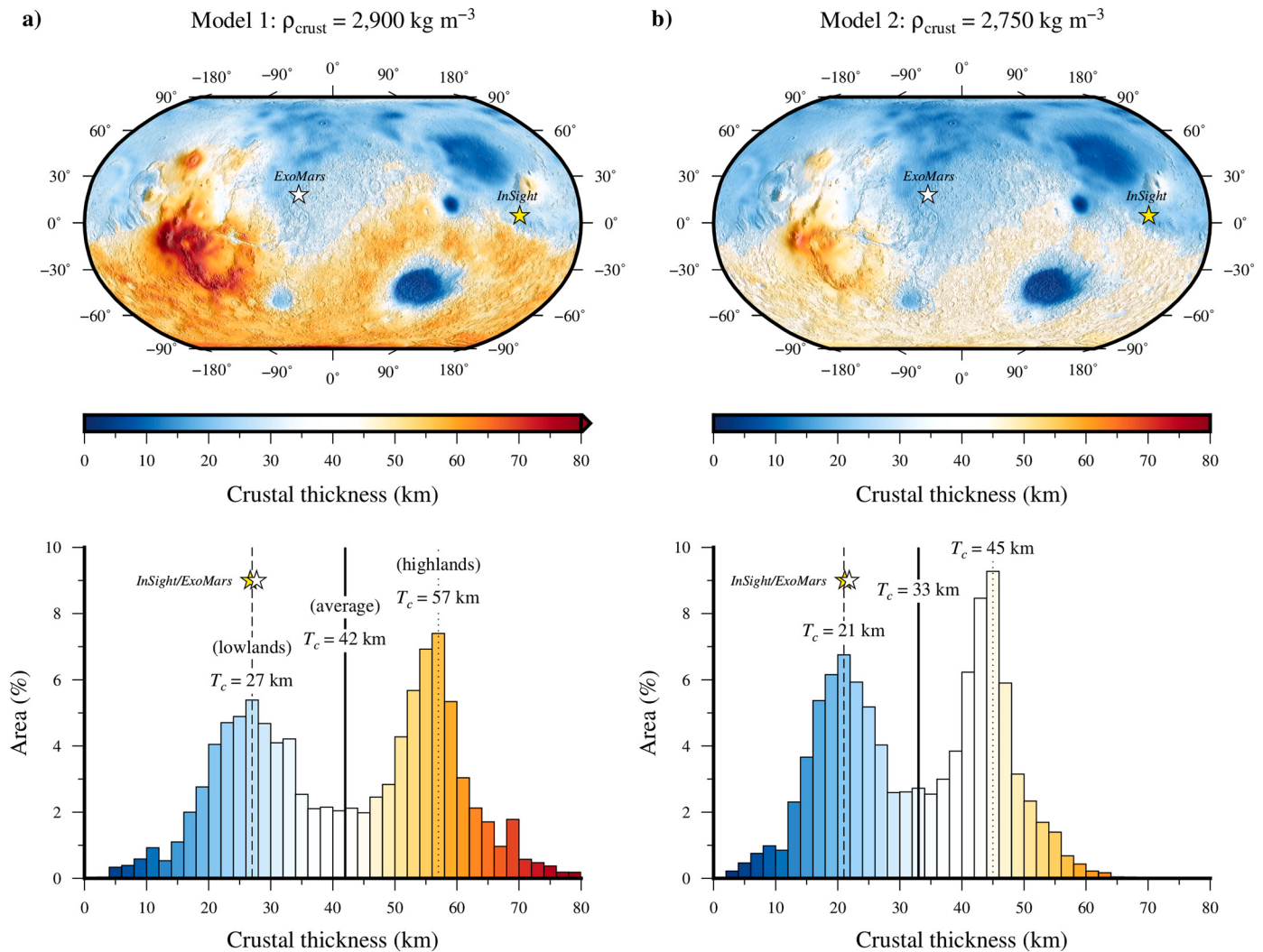


Fig. 1. Crustal thickness maps (top) and histograms of crustal thickness (bottom) for Model 1 (a) and Model 2 (b), respectively. In both crustal models, we assume a mantle density of 3500 kg m^{-3} , and the minimum crustal thickness is constrained to 1 km; yellow and white stars indicate the InSight and ExoMars landing sites (IELS). Solid, dotted, and dashed lines indicate the thicknesses of the average crust, the southern highlands, and the northern lowlands, respectively, for both crustal models considered. Stars indicate the predicted crustal thicknesses at the InSight and ExoMars landing sites. (For interpretation of the references to colour in this figure legend, the reader is referred to the web version of this article.)

thickness of the crust, and k_m is the thermal conductivity of the lithospheric mantle. We assume a mantle density of 3500 kg m^{-3} , a value widely used for Mars (e.g., Zuber et al., 2000; McGovern et al., 2002; Neumann et al., 2004; Ruiz et al., 2011). The value of H_m is poorly constrained, and here we use HPE abundances that are 0.1 times the average value for the Martian crust, consistent with a ratio between crustal and primitive mantle HPE abundances, higher than ~ 10 for Mars (Taylor and McLennan, 2009). For k_m we use the thermal conductivity of olivine according to the expression (McKenzie et al., 2005)

$$k_m = \frac{a}{1 + c(T - 273)} + \sum_{i=0}^3 d_i T^i, \quad (3)$$

where $a = 5.3$, $c = 0.0015$, $d_0 = 1.753 \times 10^{-2}$, $d_1 = -1.0364 \times 10^{-4}$, $d_2 = 2.2451 \times 10^{-7}$ and $d_3 = -3.4071 \times 10^{-11}$. Results obtained from Eq. (3) are similar to those of Hofmeister (1999) for forsterite olivine; although the upper mantle of Mars would be richer in iron content than the terrestrial one, Eq. (3) provides a good approximation, moreover when estimating the upper limits of lithospheric temperatures.

3. Strength and mechanical behavior of the lithosphere: methods

The concept of strength envelopes is useful to illustrate a first-order approximation of the variations of rheological properties of lithosphere as a function of depth (e.g., Goetze and Evans, 1979; Kohlstedt et al., 1995; Ranalli, 1997; Afonso and Ranalli, 2004). The strength of the lithosphere at any depth is the minimum between the strengths for brittle and ductile deformation.

The brittle strength is calculated, for zero-pore pressure conditions, according to the expression (e.g., Ranalli, 1997).

$$(\sigma_1 - \sigma_3)_b = \alpha \rho g z, \quad (4)$$

where $(\sigma_1 - \sigma_3)$ is the critical stress difference, the subscript b indicates brittle regime, α is a coefficient depending on the stress regime (which is 3 and 0.75 for pure compression and tension, respectively; e.g., Ranalli, 1997), ρ is the density, g is the acceleration due to gravity (3.72 m s^{-2} for Mars), and z is depth. The brittle strength of the crust is thereby calculated directly from Eq. (4) by using the crustal density. The brittle strength of the lithospheric mantle is calculated for a density of 3500 kg m^{-3}

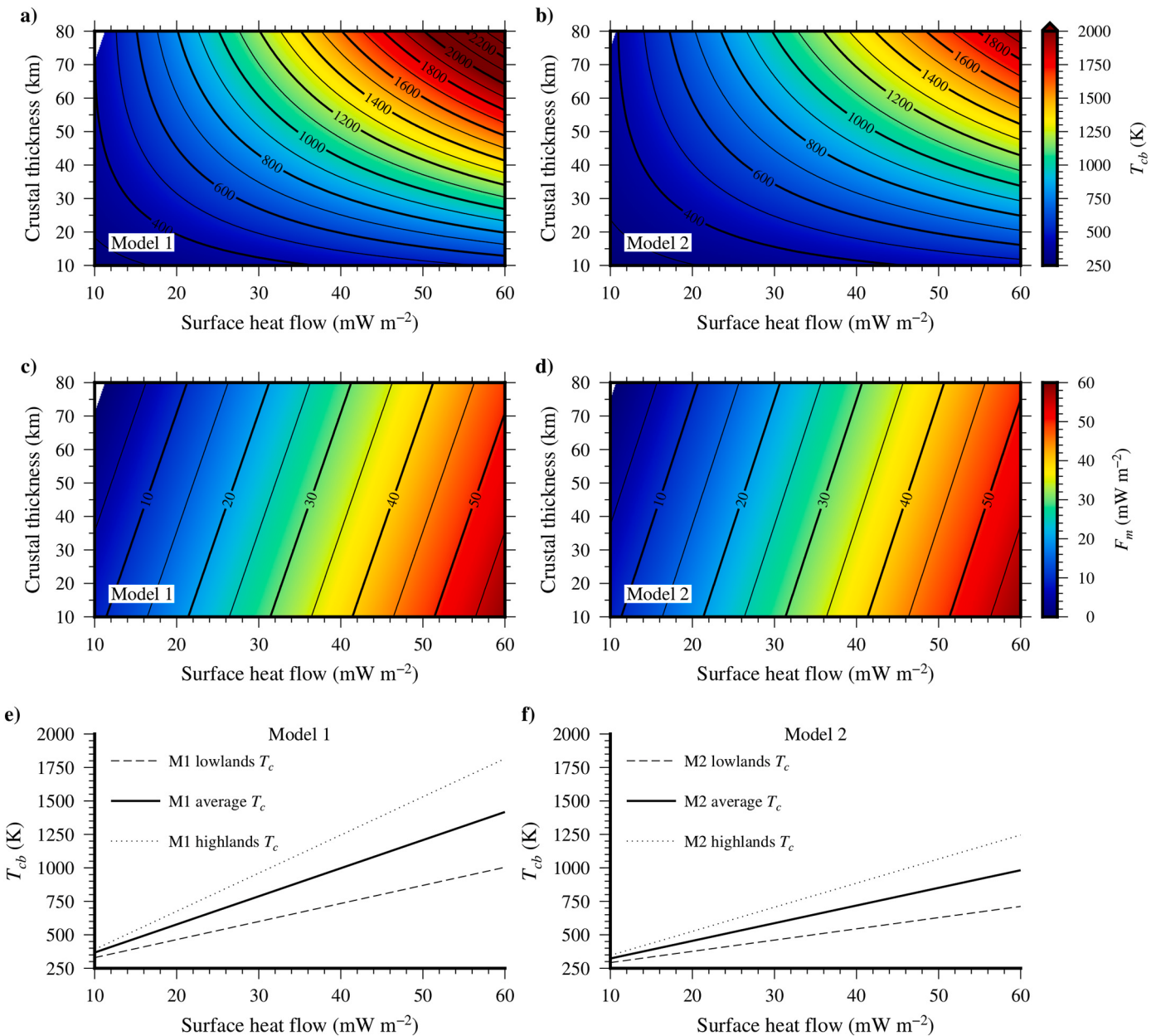


Fig. 2. (a, b) Temperature at the base of the crust T_{cb} , and (c, d) mantle heat flow F_m , as a function of surface heat flow and crustal thickness for Models 1 and 2. The white region at the upper left corresponds to negative mantle heat flow values, and hence to thermally implausible results. (e, f) T_{cb} as a function of surface heat flow for Models 1 and 2 given for crustal thicknesses representative of the average crust, the southern highlands, and the northern lowlands; the crustal thickness at the IELS is nearly identical to that representative of the northern lowlands.

m^{-3} , starting from the brittle strength at the base of the crust.

The ductile strength does not depend on the stress regime but it is strongly strain rate- and temperature-dependent, and can be described by a thermally activated power law,

$$(\sigma_1 - \sigma_3)_d = \left(\frac{\dot{\epsilon}}{A} \right)^{1/n} \exp \left(\frac{Q}{nRT} \right), \quad (5)$$

where the subscript d indicates a ductile regime, $\dot{\epsilon}$ is the strain rate, A , Q , and n are empirically-determined constants, $R (=8.31446 \text{ J mol}^{-1} \text{ K}^{-1})$ is the gas constant, and T is the absolute temperature. Here we use a strain rate of 10^{-16} s^{-1} in the calculations, based on the range usually considered for Mars (McGovern et al., 2002; Ruiz et al., 2011); this is a typical strain rate for active terrestrial plate interiors (e.g., Tesauro et al., 2007).

Even if a substantial felsic component is present, the deep crust is mostly mafic. For both crustal models, we therefore use the constants of the flow law of wet diabase: $A = 0.0612 \text{ MPa}^{-n} \text{ s}^{-1}$, $n = 3.05$ and $Q = 276 \text{ kJ mol}^{-1}$ (Caristan, 1982). The use of a wet diabase flow law is consistent with extensive evidence for water-related geological activity in early Mars (e.g., Head et al., 2001; Dohm et al., 2009); moreover, the water amount needed to “wet” the diabase is certainly modest (lower than 1%; see Caristan, 1982). The ductile strength of the mantle lithosphere is calculated for dry olivine dislocation creep rheology, by using the flow law obtained for artificially dried dunites: $A = 28840 \text{ MPa}^{-n} \text{ s}^{-1}$, $n = 3.6$ and $Q = 535 \text{ kJ mol}^{-1}$ (Chopra and Paterson, 1984).

Rocks will deform according to the weakest rheology, thus the strength of the lithosphere at any depth is given by

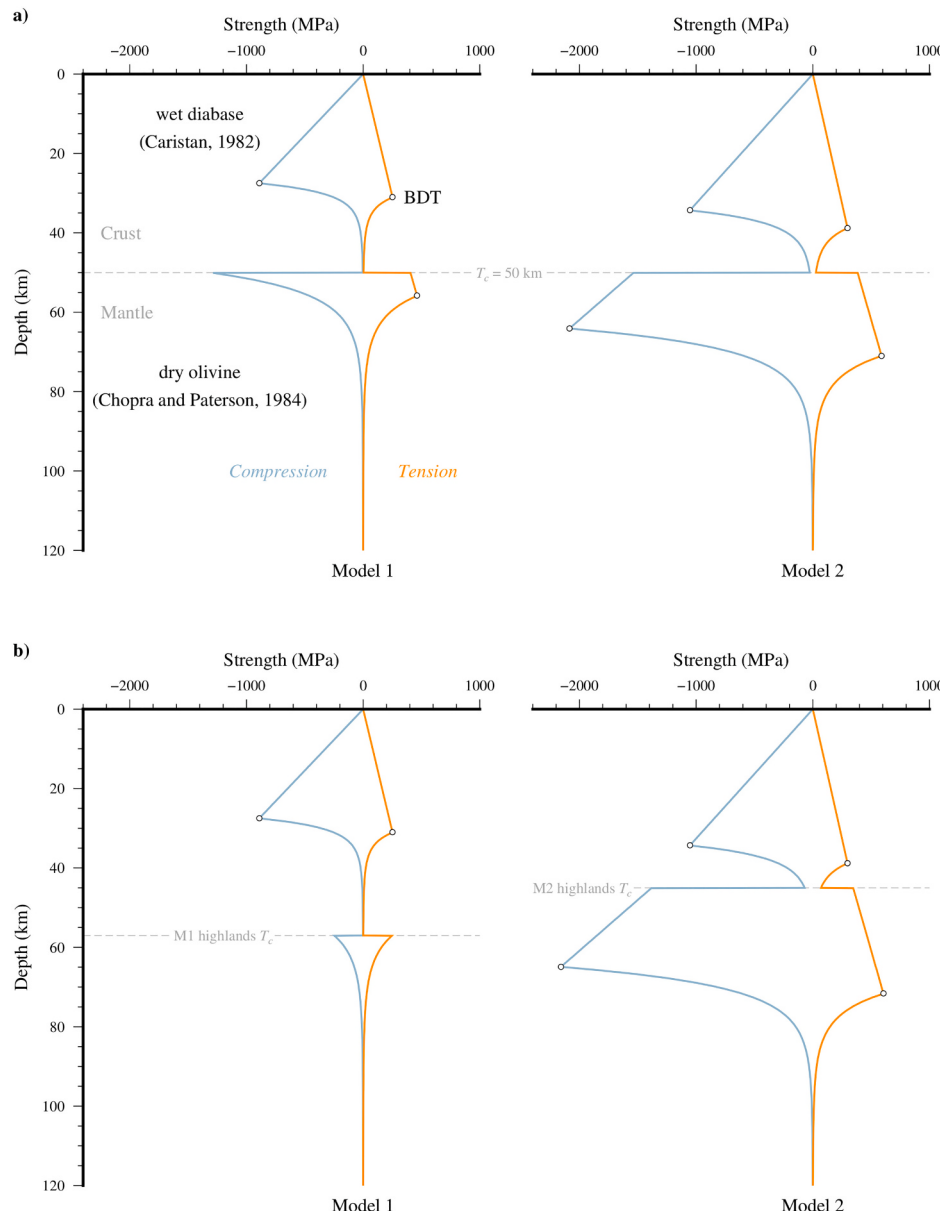


Fig. 3. (a) Comparison of strength envelopes for Model 1 and 2, for $F_s = 30 \text{ mW m}^{-2}$, $T_c = 50 \text{ km}$ and $\dot{\epsilon} = 10^{-16} \text{ s}^{-1}$. (b) Comparison of strength envelopes for the average crust of the southern highlands for Models 1 and 2. White circles denote the brittle–ductile transition (BDT).

$$(\sigma_1 - \sigma_3)(z) = \text{Min} \{ (\sigma_1 - \sigma_3)_b, (\sigma_1 - \sigma_3)_d \}, \quad (6)$$

defining the rheological profile. The total (integrated) lithospheric strength (Ranalli, 1997) can be defined as

$$S = \int_0^{T_L} (\sigma_1 - \sigma_3)(z) dz, \quad (7)$$

where $(\sigma_1 - \sigma_3)(z)$ is minor (for any given depth) between the brittle and ductile strengths as described by Eq. (6), and T_L is the mechanical thickness of the lithosphere. The base of the mechanical lithosphere is here defined as the depth at which the ductile strength reaches a low value of 10 MPa (see Ranalli, 1994; Ruiz et al., 2006a) and below which there are no further significant increases in strength. However, varying the exact value selected does not produce substantial changes in the calculations due to the exponential dependence of ductile strength on temperature (see McNutt, 1984).

The effective elastic thickness (T_e) is another kind of measure of the

total strength of the lithosphere, integrating contributions from brittle and ductile layers and from elastic cores of the lithosphere, and expressed as an equivalent purely elastic layer of homogeneous properties with thickness T_e (for a review see Burov and Diament, 1995; Watts and Burov, 2003). T_e depends on the thermal state of the lithosphere, which determines the thickness and contribution of the mechanically strong part of the lithospheric layers, and on the local curvature of the plate (which in turn depends on the rheological structure and distribution of the external loads applied to the plate; e.g., Watts and Burov, 2003; Burov and Watts, 2006). T_e can be derived from different methods, which include direct measurements of flexure from topographic data, the relationship (admittance and/or coherence) between gravimetric and topographic data in the spectral domain, or the thermo-mechanical modeling of lithospheric structure (for a review see Watts, 2001; Ruiz et al., 2006b; Kirby, 2014). If lithospheric curvature due to flexure is small, it can be neglected: in such a case, T_e can be estimated from the strength envelope (McNutt, 1984; Ruiz et al., 2010).

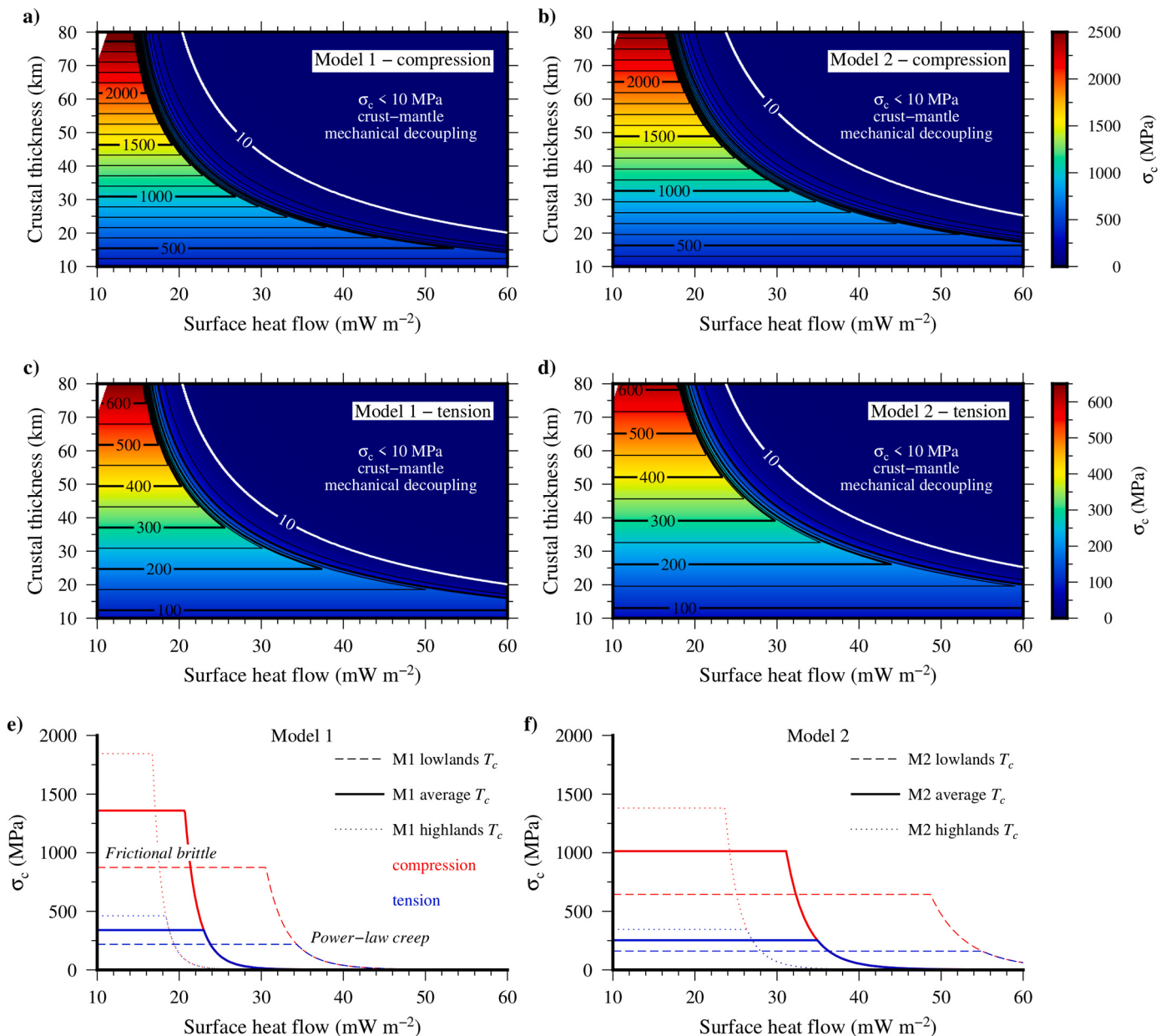


Fig. 4. (a – d) Strength at the base of the crust σ_c , as a function of surface heat flow, crustal thickness and stress regime, for both crustal models. The white line denotes the value of 10 MPa, and hence the transition from mechanical coupling of crust and mantle lithosphere to decoupling conditions. Strength scale varies from compression to tension. (e, f) Strength at the base of the crust σ_c , as a function of heat flow, for the average crust, the southern highlands, and the northern lowlands (the cases of the IELS are nearly identical to that of the northern lowlands).

Thus, for a small curvature and a mechanically welded crust and lithospheric mantle, T_e generally depends on temperature and is equal to the depth to the base of the mechanical lithosphere, T_L (see above). On the other hand, if the strength at the base of the crust is lower than 10 MPa the lithosphere is considered rheologically stratified, with a mechanically decoupled crust and lithospheric mantle; the total effective elastic thickness is then given by (Burov and Diamant, 1995)

$$T_e = (t_{ec}^3 + t_{em}^3)^{1/3}, \quad (8)$$

where t_{ec} and t_{em} are, respectively, the mechanical thicknesses of the crust and the lithospheric mantle, defined as the part of the crust or lithospheric mantle above the depth at which the ductile strength decreases to 10 MPa. If the curvature of the lithosphere is not well established, then taking T_e equal to T_L (for a welded crust and lithospheric

mantle) or as described by Eq. (8) (for a decoupled crust and lithospheric mantle) gives a robust upper limit for T_e —although some elastic stress relaxation would have taken place.

4. Surface heat flow and crustal thickness of Mars

The present-day surface heat flow on Mars might regionally reach values of up to $\sim 30 \text{ mW m}^{-2}$ (for a review see Ruiz et al., 2010; Parro et al., 2017), although higher values have been proposed taking into account possible contribution to the surface heat flow from a mantle plume beneath the Tharsis region (Grott and Breuer, 2010; Plesa et al., 2016), or more locally, due to the possible presence of a magma chamber beneath the south polar layered deposits (Sori and Bramson, 2019).

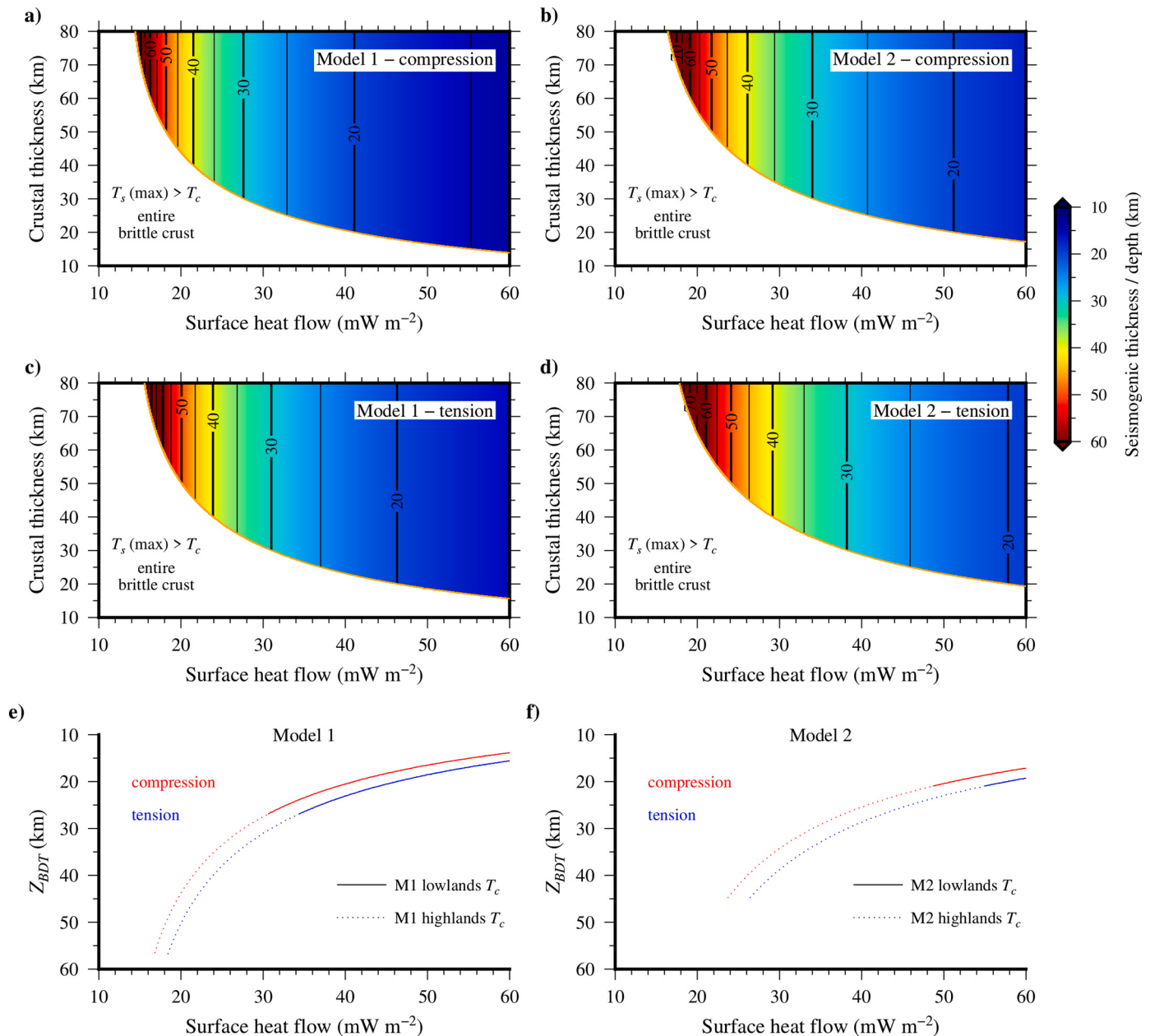


Fig. 5. (a – d) Depth to the brittle–ductile transition (Z_{BDT}) in the crust. The orange line indicates the occurrence of the brittle–ductile transition at the base of the crust. (e, f) Z_{BDT} for the southern highlands and the northern lowlands (the latter representative of the IELS).

On the other hand, the crustal thickness of Mars varies from 1 km to >100 km, depending on key assumptions in the crustal thickness modeling (Zuber et al., 2000; Neumann et al., 2004; Wieczorek and Zuber, 2004; Baratoux et al., 2014; Wieczorek, 2015; Genova et al., 2016; Goossens et al., 2017; Parro et al., 2017). In fact, these assumptions in the crustal thickness modeling may lead to significant changes in the obtained results. The most important of these assumptions is the density contrast between the mantle and crust, which affects both the overall average crustal thickness as well as the amplitude of crustal variations in our model (see Neumann et al., 2004; Baratoux et al., 2014). We therefore take into account the density dependence of the crustal structure in our models, and to do so we calculate crustal thickness models from gravity and topography (for reviews see Wieczorek and Phillips, 1998; Wieczorek, 2015), for the two crustal densities. In both crustal models, we assume a mantle density of 3500 kg m^{-3} , and the minimum crustal thickness is constrained to 1 km (see Appendix A

for further details).

The obtained crustal thickness maps for Models 1 and 2 are shown in Fig. 1 (top). Equal-area histograms of crustal thickness (Fig. 1, bottom) show their corresponding distributions. For the nominal crustal density of 2900 kg m^{-3} (Model 1), the average thickness of the crust is 42 km, and the maximum thickness is about 90 km. For the lower crustal density (Model 2), a global average value of 33 km is instead obtained, with a maximum crustal thickness of about 70 km. The global crustal structure is distinctly bimodal (e.g., Neumann et al., 2004; Plesa et al., 2016). In Model 1, the two major peaks correspond to 27 and 57 km, respectively, and in Model 2, they are 21 and 45 km, respectively. Although the northern lowlands show a broader crustal thickness distribution (see Neumann et al., 2004), we have adopted these values as representative of the southern highlands and the northern lowlands for each model as a function of crustal density. We also calculate the predicted thickness at the InSight and ExoMars landing sites (hereinafter referred to IELS) from

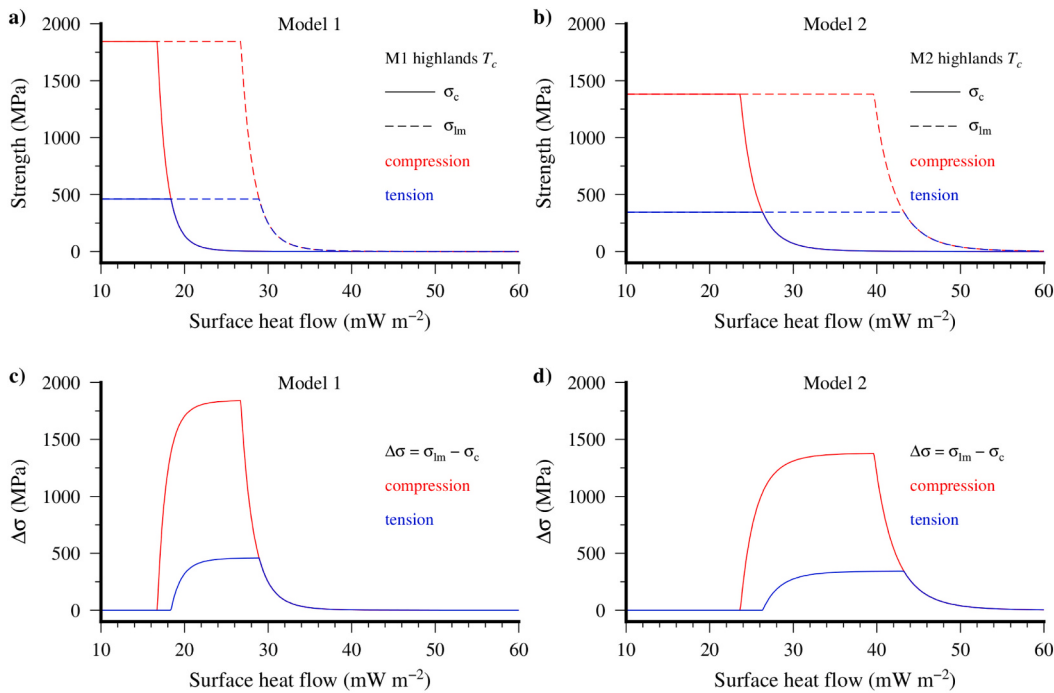


Fig. 6. (a, b) Strength at the base of the crust σ_c , and strength at the top of the lithospheric mantle σ_{lm} , as a function of the crust model and surface heat flow, for the representative crustal thickness of the southern highlands. (c, d) Strength contrast at the Moho $\Delta\sigma$, corresponding to the results in (a, b).

our models. For Model 1, the crustal thicknesses are about 27 and 28 km, respectively, whereas in Model 2, they are 21 and 22 km, respectively. We note that the predicted crustal thicknesses at IELS are very similar, as well as nearly the same as those for the northern lowlands (see Fig. 1), so hereinafter they will be considered jointly.

Thus, we examine variations of the thermal state and mechanical behavior of the lithosphere as functions of surface heat flow and crustal thickness, respectively varying between, 10 and 60 mW m⁻² and 10 and 80 km, in order to cover a wide range of states and behaviors of the lithosphere, including extreme cases (for example, possible thermal anomalies above mantle plumes) for the purposes of comparison.

5. Thermal state of the lithosphere: results

We have constructed thermal profiles from Eqs. (1)–(3) for Models 1 and 2, over a wide range of parameter values, in order to explore the effects of surface heat flow and crustal thickness on the temperature at the base of the crust (T_{cb}), and on the calculation of mantle heat flow (F_m).

Fig. 2 shows that for higher surface heat flow and/or crustal thickness the temperature at the Moho is also higher, whereas the mantle heat flow increases with increasing surface heat flow and decreases with increasing crustal thickness (and thus with a higher contribution of the crust to the surface heat flow). From Fig. 2a and b it is evident that over the whole explored range of surface heat flows and crustal thicknesses, the higher temperatures at the Moho are systematically those for Model 1, as a consequence of its lower thermal conductivity; the temperature at the base of the crust decreases slightly with the crustal density but the effect due to the thermal conductivity becomes predominant. The effect of crustal density on T_{cb} is due to the crustal heat flow component raised from assuming equal heat production by mass unit, based on Mars Odyssey GRS orbital measurements not from composition models. Note that the extreme case combining highest surface heat flows and crustal thicknesses, would result in very high temperatures at the base of the crust, reaching typical melting point values (~1273–1473 and ~973–1223 K, respectively, for basaltic and granitic rocks; see the compilation by Eppelbaum et al., 2014), and even typical values of the

thermal lithosphere–asthenosphere boundary (~1600 K for Earth; for a review see Artemieva, 2011). Fig. 2c and d show the relation between mantle heat flow, surface heat flow and crustal thickness. This relation is similar for both models, because density differences do not imply large differences in total heat production.

Fig. 2e and f show T_{cb} values for selected crustal thicknesses from each crustal model shown in Fig. 1 to facilitate comparison. In Model 2, the combined contributions of a higher thermal conductivity and a lower crustal thickness lead to significantly lower temperatures at the Moho. In particular, predicted temperatures at the base of the crust vary in the range of ~330–1000 (Model 1; Fig. 2e) and ~290–710 K (Model 2; Fig. 2f), respectively, at the InSight and ExoMars landing sites.

6. Strength and mechanical behavior of the lithosphere: results

We also systematically explore the rheology of the Martian lithosphere as a function of crustal composition. Fig. 3a shows strength envelopes for Models 1 and 2 for a surface heat flow $F_s = 30 \text{ mW m}^{-2}$ and crustal thickness $T_c = 50 \text{ km}$. Although a lower crustal density reduces the brittle strength, as is the case for Model 2, its colder geotherm, due to a higher thermal conductivity (see Section 5), leads to a stronger crust and lithospheric mantle, and therefore to a thicker lithosphere. It also leads to a stronger lithosphere as a whole in terms of total strength and effective elastic thickness, as a consequence of higher crust and mantle contributions to the strength of the lithosphere. (Note that the use of a dry rheology for the upper mantle implies an upper limit for lithospheric strength.). This effect is more pronounced when taking into account the differences in crustal thickness at one specific location for the different crustal models (see for example the case of the southern highlands; Fig. 3b). Some of these issues will be examined in more detail in the following subsections.

6.1. Strength at the base of the crust

The possible mechanical decoupling between the Martian crust and lithospheric mantle is largely controlled by the strength of the lower crust, and thus investigating the strength at the base of the crust is very

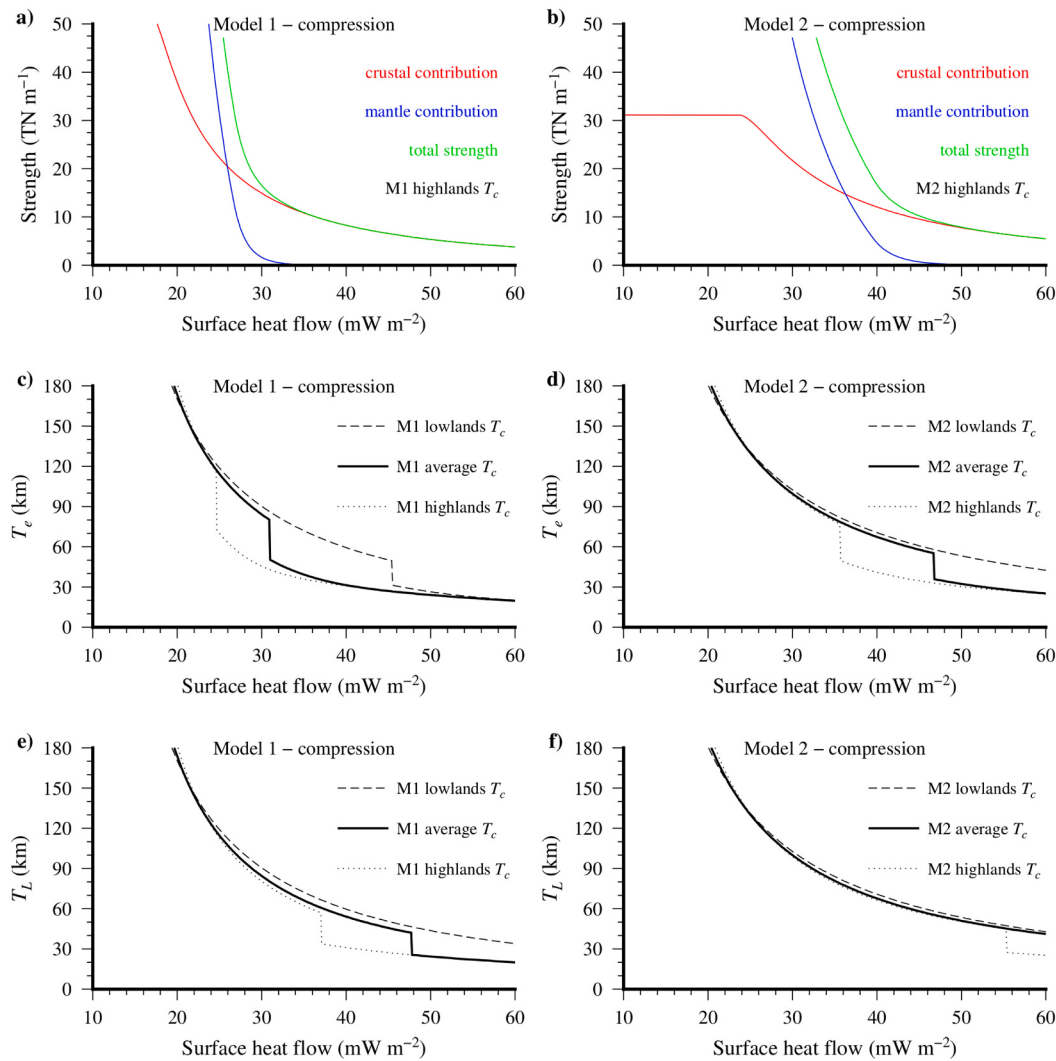


Fig. 7. (a, b) Contribution of the crust (red line) and of the lithospheric mantle (blue line) to the total strength of the lithosphere (green line), as a function of the crust model and surface heat flow, for the southern highlands. (c, d) Effective elastic thickness of the lithosphere T_e , for the average crust, the southern highlands, and the northern lowlands (the cases of the IELS are nearly identical to that of the northern lowlands). (e, f) Mechanical thickness of the lithosphere T_L . Panel format is the same as (c, d). (For interpretation of the references to colour in this figure legend, the reader is referred to the web version of this article.)

informative to assess this point. Fig. 4 shows the strength at the base of the crust (σ_c) as a function of the composition of the crust, surface heat flow, crustal thickness and stress regime (Fig. 4e and f show σ_c for selected crustal thicknesses). The trends for both crustal models are very similar. If the temperature at the base of the crust is lower than the temperature of the brittle–ductile transition, then the brittle strength is dominant, and σ_c keeps a constant value for a limited range of surface heat flows. Under the same conditions, σ_c increases with increasing crustal thickness (being higher for compression) as predicted by Eq. (4), and for Model 1 as a consequence of its higher crustal density. If the temperature at the base of the crust is higher than the temperature of the brittle–ductile transition, the ductile strength becomes predominant and σ_c decreases drastically with increasing temperature as a consequence of the exponential dependence between strength and temperature predicted by Eq. (5). Under the threshold of 10 MPa, we therefore consider mechanical decoupling between the crust and lithospheric mantle.

In general, brittle deformation predominates at the base of thin crusts for a wide interval of surface heat flows, whereas the base of thick crusts will deform mainly in a ductile way. Due to a slightly higher absolute value of the brittle strength in Model 1 with respect to Model 2, combined with a hotter geotherm, the ductile strength in Model 1 is

dominant for a larger range of surface heat flows and crustal thicknesses, as well as the conditions in which the crust and lithospheric mantle are decoupled (see also Fig. 3). Fig. 4e and f allow us to summarize rheological behaviors that result from those different scenarios. The most noticeable difference between both crustal models is observed in the northern lowlands: In Model 2, the brittle strength is dominant for a larger range, and the crust and lithospheric mantle remain mechanically welded even for the largest surface heat flow values considered here.

6.2. Depth to the brittle–ductile transition (BDT) within the crust: Seismogenic layer thickness (T_s)

The brittle–ductile transition (BDT) indicates the depth at which brittle and ductile strength are equal. Above this depth (Z_{BDT}), rocks deform by brittle failure, while below this depth, rocks experience ductile deformation (see Section 3). The BDT controls the potentially maximum extent of faulting (i.e., the seismogenic thickness, T_s) in the uppermost, competent part of the lithosphere (for reviews see Watts and Burov, 2003; Burov and Watts, 2006). Thus, the BDT is a key feature for understanding the mechanisms of dike propagation, magma transport, and groundwater storage/circulation, through the Martian lithosphere

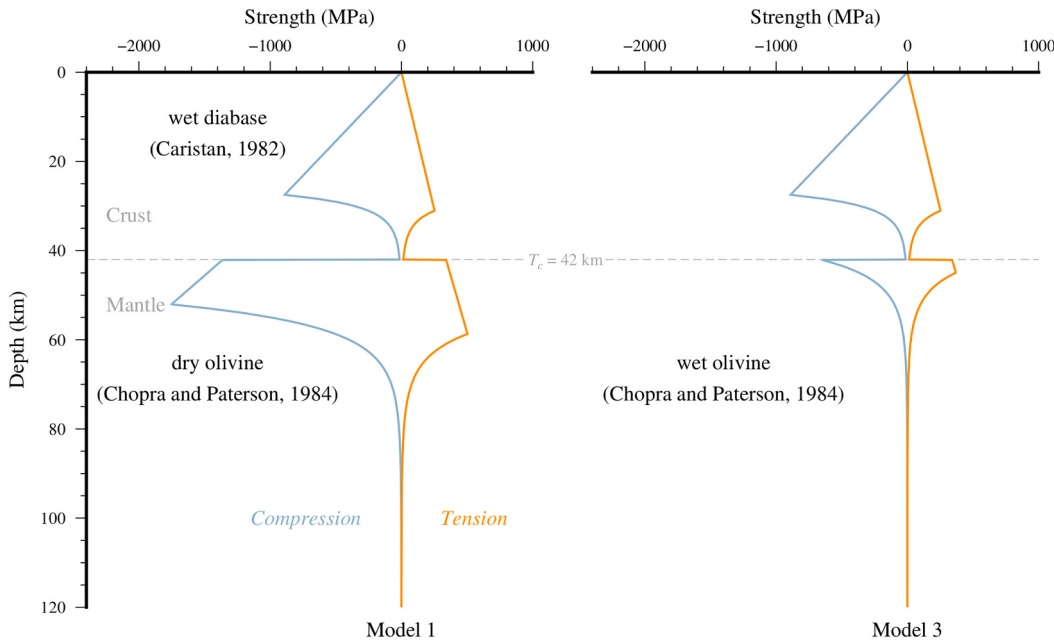


Fig. 8. Comparison of strength envelopes calculated for dry (left, Model 1) and wet (right, Model 3) olivine creep rheologies, for $F_s = 30 \text{ mW m}^{-2}$ and $T_c = 42 \text{ km}$.

(e.g., Heap et al., 2017), in addition to the recent and current seismic activity on Mars (e.g., Senthil Kumar et al., 2019), leading to a better understanding of observations by the SEIS instrument of the Insight Mission (Lognonné et al., 2019).

Z_{BDT} is strongly dependent on temperature for a given composition and stress regime due to the exponential function that describes ductile strength. Fig. 5 shows how Z_{BDT} varies in the crust as a function of surface heat flow and crustal thickness for Models 1 and 2 and for different stress regimes. The white region on the plots of Fig. 5 indicates that the entire crust in that region deforms in a brittle way (i.e., there is no BDT in the crust) and therefore the BDT is in fact located deeper—in the brittle part of the uppermost mantle.

Lower values of F_s imply lower crustal temperatures, which result in an increase in ductile strength and the prevalence of the brittle domain in deeper areas; and therefore deeper BDT values: for thinner crusts, the brittle behavior persists throughout the whole crust and there is no BDT in the crust. As surface heat flow increases, the temperature rises and the ductile strength diminishes, so the BDT is located at shallower depths. In this case, if the upper lithospheric mantle is still brittle, then there will be two main seismogenic layers, one in the uppermost crust and the other in the uppermost mantle, separated by an aseismic region (see Watts and Burov, 2003; Burov and Watts, 2006) (see Fig. 3 herein). For a fixed F_s , the BDT is not a function of T_c , although a minimum value of T_c is necessary to establish a BDT in the crust.

Fig. 5e and f show how Z_{BDT} varies within the crust of the southern highlands and the northern lowlands and IELS. In Model 1, a hotter crust in the ductile regime leads to shallower BDT depths than for Model 2 (see also Fig. 3), and hence to a thinner seismogenic layer. Furthermore, in Model 2, the entire crust in the northern lowlands (and therefore the IELS) remains brittle for a larger range of surface heat flows, as we noted in the previous subsection.

6.3. Crust composition and mechanical strength of the lithosphere

The rheological contrast at the Moho is a useful indicator of the first-

order rheological structure of the lithosphere (for a review see Ranalli and Adams, 2013). The strength contrast at the Moho can be defined as.

$$\Delta\sigma = \sigma_{lm} - \sigma_c, \quad (9)$$

where σ_c and σ_{lm} are, respectively, the strength at the base of the crust and at the top of the lithospheric mantle. Fig. 6 shows the strength and the change of predominant deformation mechanisms immediately above and below the Moho, as well as the strength contrast, for the southern highlands. For low surface heat flows, the brittle strength is dominant above and below the Moho, and therefore $\Delta\sigma = 0$. As the temperature at the base of the crust increases, the ductile strength becomes predominant in the lower crust and σ_c decreases drastically, whereas the upper lithospheric mantle is still brittle and σ_{lm} remains constant. $\Delta\sigma$ therefore increases drastically until reaching its maximum value when σ_c becomes negligible. Finally, the ductile strength becomes predominant in the upper lithospheric mantle, σ_{lm} decreases drastically with increasing temperature, and hence $\Delta\sigma$ decreases to negligible values. While the absolute value of the strength contrast at the Moho is higher in Model 1, this large strength contrast between the crust and mantle exists for a larger range of conditions in Model 2 due to its influence on the strength of the crust and lithospheric mantle (see below).

Fig. 7a and b show the contributions of the crust and of the lithospheric mantle to the total strength of the lithosphere for the southern highlands. Although the lower crustal thickness of Model 2 limits the maximum contribution of the crust to the total strength of the lithosphere, this model results in a stronger lithosphere as a whole. Fig. 7c and d show estimates of the total strength of the lithosphere based on T_e calculated from lithosphere strength (by assuming zero plate curvature, giving thus an upper limit for T_e) for selected crustal thicknesses. The higher crust and mantle contributions to the strength of the lithosphere lead to significantly higher T_e values. For each crustal thickness, the calculated T_e decreases gradually with increasing crustal temperatures, which are a function of heat flow. As heat flow increases, the strength in the lower crust decreases until reaching negligible values, leading to mechanical decoupling between the crust and the lithospheric mantle,

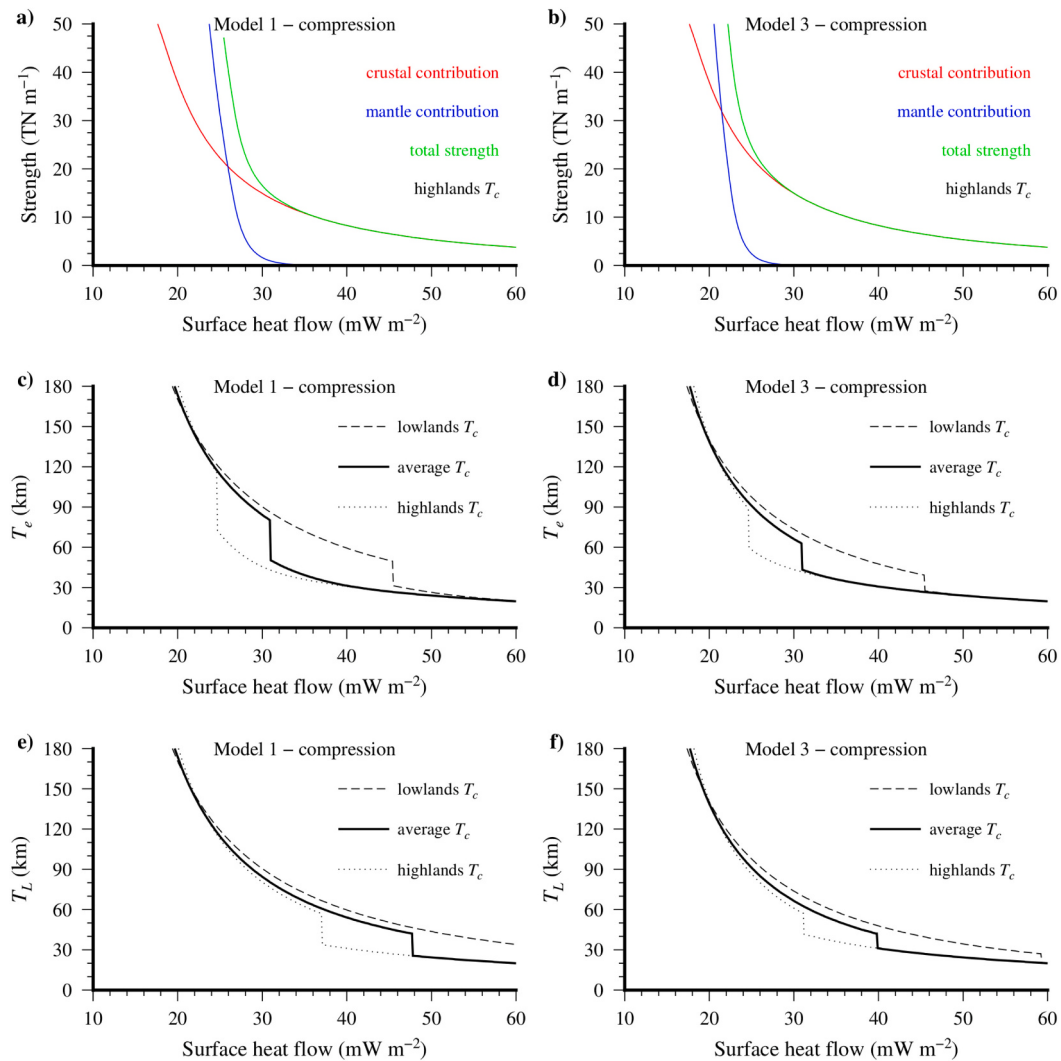


Fig. 9. (a, b) Contribution of the crust (red line) and of the lithospheric mantle (blue line) to the total strength of the lithosphere (green line), as a function of the rheology of the lithospheric mantle and surface heat flow, for the southern highlands. (c, d) Effective elastic thickness of the lithosphere T_e , for the average crust, the southern highlands, and the northern lowlands. (e, f) Mechanical thickness of the lithosphere T_L . Panel format is the same as (c, d). (For interpretation of the references to colour in this figure legend, the reader is referred to the web version of this article.)

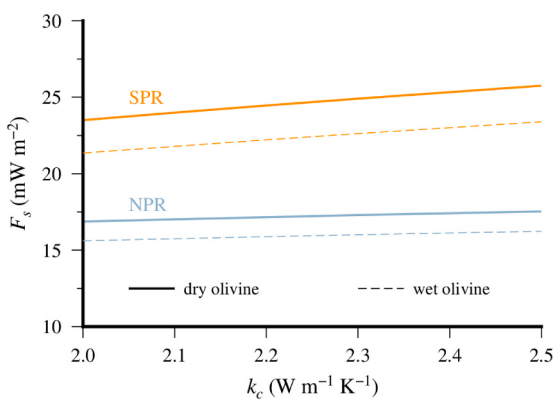


Fig. 10. Present-day surface heat flow from the effective elastic thickness of the lithosphere (T_e) at the North and South Polar regions (NPR and SPR, respectively) as a function of crustal thermal conductivity, for dry and wet olivine creep rheologies.

and hence to a drastic reduction in T_e (marked by the jump in Fig. 7c and d). Crust–mantle mechanical decoupling is dominant for a larger range of conditions in Model 1 (see Fig. 4), and this drastic reduction in T_e is present in all three cases. However, in Model 2, the crust and lithospheric mantle of the northern lowlands and IELS remain mechanically welded across the entire range of surface heat flow, exhibiting the highest T_e values. Finally, when the strength of the lithospheric mantle decreases and becomes nil or negligible, then T_e becomes controlled by the crust, being slightly higher in Model 2.

Fig. 7e and f show the mechanical thickness of the lithosphere (T_L) given selected crustal thicknesses for the southern highlands and the northern lowlands. For low surface heat flows, the base of the mechanical lithosphere becomes controlled by the mantle, and therefore Model 2 results in a thicker lithosphere for all cases as a consequence of its colder geotherm. As heat flow (crustal temperature) increases, the strength of the lithospheric mantle decreases and becomes nil or negligible, and the mechanical thickness of the lithosphere becomes controlled by the crust, leading to a drastic reduction in T_L (jump in Fig. 7e and f). Note that, in this case, the base of the mechanical lithosphere is shallower than the own base of the crust, i.e., T_L corresponds to

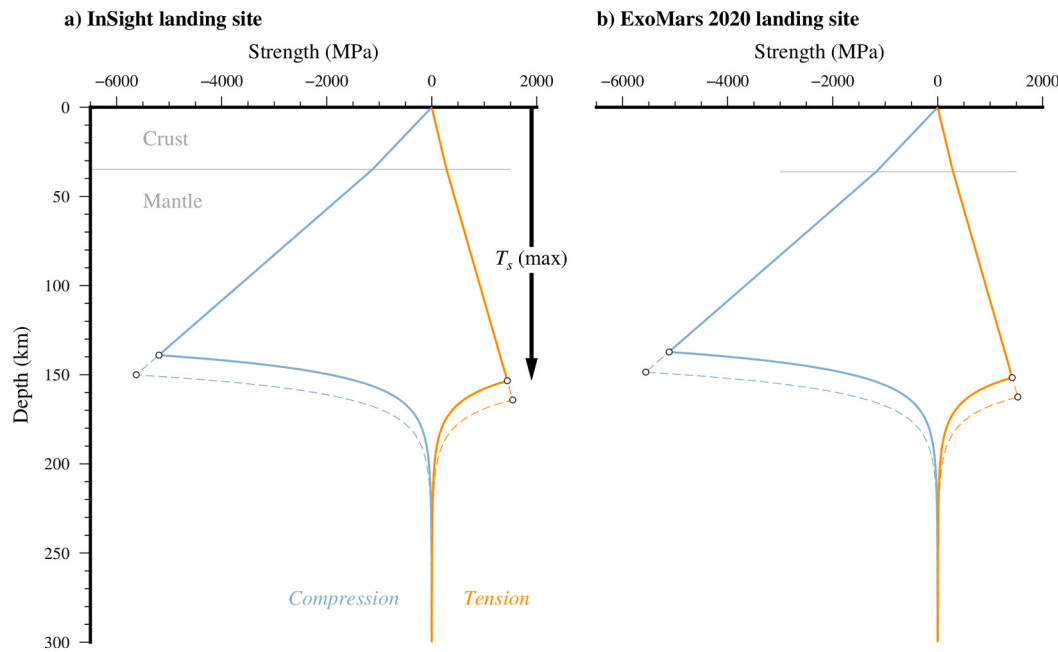


Fig. 11. Strength envelopes at the InSight and ExoMars landing sites calculated using crustal thickness and surface heat flow values for each location obtained from the models by Parro et al. (2017). Thick solid lines show the results from the nominal model, which is equivalent to Model 1. Thin dashed lines show the results from the end-member model, which considers a higher crustal thermal conductivity similar to Model 2. White circles denote the brittle–ductile transition (BDT).

the thickness of the mechanically strong layer of the crust (e.g., Anguita et al., 2001), which again is slightly higher in Model 2.

6.4. A note on the effect of water content on lithospheric mantle

Water content in the Martian interior is not well constrained, but some studies suggest that the mantle could store a substantial amount of water (Wade et al., 2017). Mantle water content may have a large influence on the rheological properties of the lithospheric mantle due to the water weakening effect (for a review see Kohlstedt and Mackwell, 2010). Moreover, water weakening may play a significant role in the more iron-rich mantle of Mars because water solubility increases with increasing iron content (Zhao et al., 2004; Withers et al., 2011).

Here we compare dry (Model 1) and wet (Model 3) olivine dislocation creep rheologies (see Fig. 8). Model 3, which has crustal parameters similar to Model 1, uses the constants for the flow law of the Anita Bay dunite: $A = 9550 \text{ MPa}^{-n} \text{ s}^{-1}$, $n = 3.35$ and $Q = 444 \text{ kJ mol}^{-1}$ (Chopra and Paterson, 1984). This flow law places a lower limit on the strength of wet olivine due to its relative weakness (compared with other wet dunites, such as Aheim dunite). Fig. 9 shows the total strength, effective elastic thickness, and mechanical thickness of the lithosphere for selected crustal thicknesses. A wet rheology implies a substantial reduction of the mantle contribution to the total strength and effective elastic thickness of the lithosphere, resulting in a significantly weaker lithosphere as a whole (see for example, Ruiz et al., 2008, 2011; Grott and Breuer, 2009; Thiriet et al., 2018). In addition, a wet olivine rheology results in a thinner lithosphere when its mechanical thickness becomes controlled by the mantle.

7. Discussion and conclusions

The existent link between material properties, thermal structure, and mechanical behavior of the lithosphere permits that inferences obtained

for one of these aspects can be used in order to gain knowledge of the others. Thus, our detailed evaluation can be used as a guide for improving the interpretation of geophysical or geological data, as those expected to be acquired by ExoMars 2020 and InSight, or future (orbit- or ground-based), missions. Next, we discuss two important points for which we consider the results here presented as relevant to the geophysical exploration of Mars.

Effective elastic thickness estimates can be converted to estimates of heat flow using the relationship between lithospheric strength, deflection caused by loading, and thermal structure; this relation is described through the strength envelope procedure detailed by McNutt (1984). Thus, variations of the effective elastic thickness may reflect differences in the local lithospheric thermal regime (for reviews see Ruiz et al., 2011; Ruiz, 2014). The loading of the lithosphere of the polar regions by the northern and southern polar caps has allowed the estimation of their respective effective elastic thicknesses (which were proposed to be higher than 300 and 161 km, respectively; Phillips et al., 2008; Wieczorek, 2008), and hence to derive estimates of the present-day surface heat flow (Ruiz et al., 2010, 2011; Parro et al., 2017), because polar caps, and their associated loading, are recent features (Laskar et al., 2002; Phillips et al., 2008). The thermal conductivity of the crust could influence the calculation of heat flows at the North (NPR) and South (SPR) Polar regions. The nominal thermal conductivity used by Ruiz et al. (2011) and Parro et al. (2017) was a typical basalt value of $2 \text{ W m}^{-1} \text{ K}^{-1}$. For the felsic terrestrial continental upper crust a thermal conductivity of $2.5 \text{ W m}^{-1} \text{ K}^{-1}$ is frequently used, although a recent revision (Jaupart et al., 2016) has found that the thermal conductivity of felsic rocks in the terrestrial crust is usually not significantly higher than $2 \text{ W m}^{-1} \text{ K}^{-1}$: because a thermal conductivity of $2 \text{ W m}^{-1} \text{ K}^{-1}$ is an upper limit for basaltic rocks; the use of this value could also be roughly consistent with a basaltic crust with a felsic component.

In any case, to illustrate the effect of a higher thermal conductivity, Fig. 10 shows the surface heat flow calculated for the NPR and SPR

following the methodology by Parro et al. (2017), as a function of the crustal thermal conductivity. The low (or nonexistent) surface deflection in these regions (Phillips et al., 2008) permits us to assume zero plate curvature. In both cases, the obtained surface heat flow increases with increasing crustal thermal conductivity because, under the same conditions, a higher crustal thermal conductivity results in a colder geotherm and hence in a higher T_e (see Section 6). Thus, higher surface heat flows are required for matching a given T_e as the crustal thermal conductivity increases. It can be seen that the effect of crustal thermal conductivity is comparatively limited (<10%) in both cases, due to the larger contribution from the mantle to mechanical thickness of the lithosphere. For this reason, the heat flow results by Ruiz et al. (2010, 2011) and Parro et al. (2017) are reliable and scarcely dependent on the exact composition of the Martian crust.

The brittle–ductile transition (BDT) controls the potentially maximum extent of faulting (i.e., the seismogenic thickness) in the uppermost, competent part of the lithosphere (for a review see Watts and Burov, 2003; Burov and Watts, 2006). Thus, the BDT is a key feature for understanding the recent and current seismic activity on Mars (e.g., Senthil Kumar et al., 2019), as well as for a better understanding of observations by the SEIS instrument (Plesa et al., 2018; Lognonné et al., 2019). Our results show how the composition of the crust (modeled here through the crustal thermal conductivity and density) has a large influence not only on the rheological behavior of the crust, but also on the strength of the lithospheric mantle. Model 2 results in a significantly stronger crust and lithospheric mantle than Model 1 under the same conditions, as a consequence of its colder geotherm. This implies that marsquakes could be deeper for Model 2, but because of a stronger lithosphere, probably more infrequent. Fig. 11 shows strength envelopes for the InSight and ExoMars landing sites calculated using crustal thickness and surface heat flow values for each location obtained from the models by Parro et al. (2017). From their nominal model (which has crustal parameters similar to Model 1), the predicted maximum seismogenic thickness varies in the range of ~140–155 and ~135–150 km, respectively, depending on the stress regime. These thicknesses increase when considering a higher crustal thermal conductivity by using their end-member model (similar to Model 2). Thus, comparison of InSight measurements with our estimates for BDT depth and total strength will serve to relate them with crustal and mantle material and heat flow.

Summarizing, our investigation of the effects of crust properties on the thermal and mechanical structure of the Martian lithosphere under a

wide range of conditions show that the crustal composition (in terms of crustal density and thermal conductivity) has a strong control over the thermal state of the entire lithosphere, and thereby over the strength of the lithospheric mantle. This even may result in a stronger lithosphere as a whole in terms of total strength and effective elastic thickness due to higher crust and mantle contributions to lithospheric strength. On the other hand, we have also shown that water content has a large effect on the rheology of the upper mantle. A wet rheology implies a substantial reduction of the mantle contribution to the total strength and effective elastic thickness of the lithosphere, resulting in a significantly weaker lithosphere as a whole. Our results will therefore serve both to improve our understanding of geophysical observations from the InSight and ExoMars missions and to further constrain theoretical modeling efforts.

Acknowledgments

We thank two anonymous reviewers for their constructive reviews that improved this manuscript, and guest editor Miguel Ángel López-Valverde for handling our manuscript. Crustal thickness models were obtained using the SHTools software package (Wieczorek and Meschede, 2018). All figures were generated using the Generic Mapping Tools (GMT) package (Wessel et al., 2013). This research has received funding from the European Union's Horizon 2020 Programme (H2020-Compet-08-2014) under grant agreement UPWARDS-633127, from the Santander-UCM project PR75/18-21613 (AMARTE2), and from the project PGC2018-095340-B-100 (TECTOMARTE), funded by the Spanish Ministry of Science, Innovation and Universities, the Spanish State Research Agency and the European Regional Development Fund (MCIU/AEI/FEDER, UE). The work by A.J.-D. was supported by a Juan de la Cierva-Formación postdoctoral contract (ref. FJCI-2016-28878) from the Spanish Ministry of Science, Innovation and Universities and the Spanish State Research Agency. I.E.-G. is grateful to the Universidad de Cádiz for supporting this work through the project PR2017-074. The work by L.M.P. was supported by a FPU grant (ref. 2014/04842) from the Spanish Ministry of Science, Innovation and Universities. L.M.P. is a Graduate Fellow of the Madrid City Council (Spain) at the Residencia de Estudiantes, 2018–2020. The work by M.T. was supported by the Japan Society for the Promotion of Science (18K13634). The manuscript has been carefully revised by Grant George Buffet (a physical scientist and native English speaking editor) to improve its grammar and readability (www.terranova.barcelona).

Appendix A. Crustal thickness of Mars: density dependence of the crustal structure

In order to take into account the density dependence of the crustal structure in our models (see Neumann et al., 2004; Baratoux et al., 2014), we calculate crustal thickness models for the two crustal densities considered here. For this, we use the relationship between global topography and gravity to model the crustal thickness (T_c) of Mars following the potential theory procedure of Wieczorek and Phillips (1998). To constrain the thickness of the Martian crust, we assume (1) that the observed gravitational anomalies arise only from relief along the surface and crust–mantle interface, and (2) constant crustal and mantle densities to overcome the non-uniqueness associated with potential modeling. We use the spherical harmonic shape model MarsTopo2600 (Wieczorek, 2015) and the GMM-3 gravity model (Genova et al., 2016), both truncated at degree $l = 90$ in our analysis. For Models 1 and 2, we assume a crustal density of 2900 and 2750 kg m⁻³, respectively (see the main text for further details). In both crustal models, we assume a mantle density of 3500 kg m⁻³, and we constrained the minimum crustal thickness to 1 km. Under these assumptions, we first calculate the Bouguer gravity anomaly from surface topography and the free air anomaly, and then calculate by downward continuation the shape of the crust–mantle interface necessary to minimize the difference between the observed and predicted Bouguer anomalies (for reviews see Wieczorek and Phillips, 1998; Wieczorek, 2015). In order to mitigate errors in the downward continuing Bouguer anomaly, we applied a minimum amplitude filter (see Wieczorek and Phillips, 1998) for the Moho relief at degree $l = 50$. Finally, we obtain the crustal thickness by subtracting the relief of the Moho from the surface topography. Crustal thickness maps for Models 1 and 2 are presented in Fig. 1.

Additionally, we explore the dependence of crustal structure on crustal density. We calculate crustal thickness models for crustal densities ranging from 2400 to 3250 kg m⁻³ in increments of 50 kg m⁻³ (see Baratoux et al., 2014). Here we consider a generous lower bound for the crustal density in order to take into account the lower average bulk crustal density (2582 ± 209 kg m⁻³) obtained by Goossens et al. (2017). For each crustal thickness inversion, we assume a mantle density of 3500 kg m⁻³ and the minimum crustal thickness is constrained to 1 km. Fig. A1 shows the average and maximum crustal thicknesses as a function of crustal density, as well as the predicted crustal thicknesses at the InSight and ExoMars landing sites.

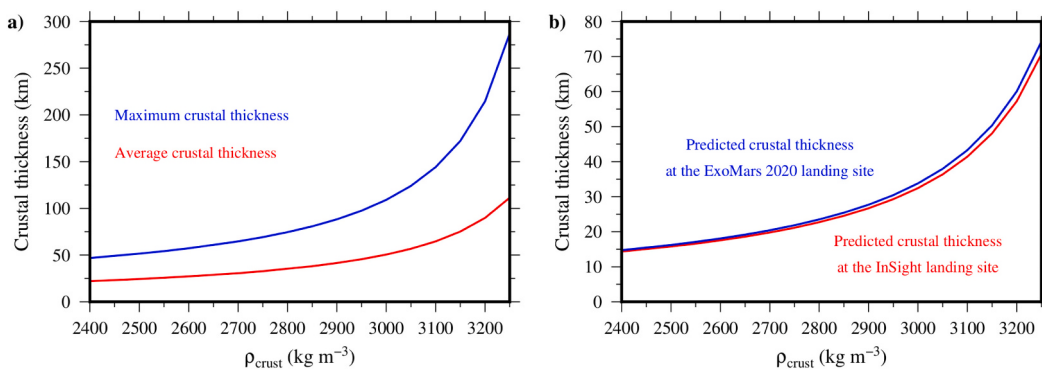


Fig. A1. Average and maximum crustal thickness (a) and predicted crustal thickness at the InSight and ExoMars landing sites (b) as a function of crustal density. We assume a mantle density of 3500 kg m^{-3} and the minimum crustal thickness is constrained to 1 km.

References

- Afonso, J.C., Ranalli, G., 2004. Crustal and mantle strengths in continental lithosphere: is the jelly sandwich model obsolete? *Tectonophysics* 394, 221–232.
- Anguita, F., et al., 2001. Tharsis dome, Mars: new evidence for Noachian-Hesperian thick-skin and Amazonian thin-skin tectonics. *J. Geophys. Res.* 106 (E4), 7577–7589.
- Artemieva, I., 2011. *The Lithosphere: An Interdisciplinary Approach*. Cambridge University Press, Cambridge (773 pp).
- Banerdt, W.B., Russell, C.T., 2017. Editorial on: topical collection on InSight mission to Mars. *Space Sci. Rev.* 211, 1–3. <https://doi.org/10.1007/s11214-017-0414-0>.
- Baratoux, D., et al., 2014. Petrological constraints on the density of the Martian crust. *J. Geophys. Res.* 119, 1707–1727.
- Beardsmore, G.R., Cull, J.P., 2001. *Crustal Heat Flow: A Guide to Measurement and Modelling*. Cambridge University Press, Cambridge (324 pp).
- Burov, E.B., Diament, M., 1995. The effective elastic thickness of (Te) continental lithosphere. What does it really mean? *J. Geophys. Res.* 100 (B3), 3905–3927.
- Burov, E.B., Watts, A.B., 2006. The long-term strength of continental lithosphere: “jelly sandwich” or “crème brûlée”? *GSA Today* 16 (1), 4–10.
- Caristan, Y., 1982. The transitions from high temperature creep to fracture in Maryan diabase. *J. Geophys. Res.* 87, 6781–6790.
- Carter, J., Poulet, F., 2013. Ancient plutonic processes on Mars inferred from the detection of possible anorthositic terrains. *Nat. Geosci.* 6, 1008–1012.
- Chopra, P.N., Paterson, M.S., 1984. The role of water in the deformation of dunite. *J. Geophys. Res.* 89, 7861–7876.
- Dohm, J.M., et al., 2009. GRS evidence and the possibility of paleooceans on Mars. *Planet. Space Sci.* 57, 664–684.
- Egea-González, I., et al., 2017. Thrust fault modeling and Late-Noachian lithospheric structure of the circum-Hellas region, Mars. *Icarus* 288, 53–68.
- Fountain, D.M., Salisbury, M.H., Percival, J., 1990. Seismic structure of the continental crust based on rock velocity measurements from the Kapuskasing uplift. *J. Geophys. Res.* 95 (B2), 1167–1186. <https://doi.org/10.1029/JB095iB02p01167>.
- Frey, H.V., 2006. Impact constraints on, and a chronology for, major events in early Mars history. *J. Geophys. Res.* 111, E08S91. <https://doi.org/10.1029/2005JE002449>.
- Genova, A., et al., 2016. Seasonal and static gravity field of Mars from MGS, Mars odyssey and MRO radio science. *Icarus* 272, 228–245.
- Goetze, C., Evans, B., 1979. Stress and temperature in the bending lithosphere as constrained by experimental rock mechanics. *Geophys. J. R. Astron. Soc.* 59, 463–478. <https://doi.org/10.1111/j.1365-246X.1979.tb02567.x>.
- Golombek, M., Kipp, D., Warner, N., et al., 2017. Selection of the InSight landing site. *Space Sci. Rev.* 211, 5. <https://doi.org/10.1007/s11214-016-0321-9>.
- Golombek, M., Grott, M., Kargl, G., et al., 2018. Geology and physical properties investigations in the InSight Lander. *Space Sci. Rev.* 214, 84. <https://doi.org/10.1007/s11214-018-0512-7>.
- Goossens, S., et al., 2017. Evidence for a low bulk crustal density for Mars from gravity and topography. *Geophys. Res. Lett.* 44, 7686–7694.
- Grott, M., Breuer, D., 2009. Implications of large elastic thicknesses for the composition and current thermal state of Mars. *Icarus* 201, 540–548.
- Grott, M., Breuer, D., 2010. On the spatial variability of the Martian elastic lithosphere thickness: evidence for mantle plumes? *J. Geophys. Res.* 115, E03005 <https://doi.org/10.1029/2009JE003456>.
- Grott, M., et al., 2005. High heat flux on ancient Mars: evidence from rift flank uplift at Coracis Fossae. *Geophys. Res. Lett.* 32, L21201 <https://doi.org/10.1029/2005GL023894>.
- Grott, M., et al., 2007. Mechanical modelling of thrust faults in the Thaumasia region, Mars, and implications for the Noachian heat flux. *Icarus* 186, 517–526.
- Hahn, B.C., McLennan, S.M., Klein, E.C., 2011. Martian surface heat production and crustal heat flow from Mars odyssey gamma-ray spectrometry. *Geophys. Res. Lett.* 38, L14203. <https://doi.org/10.1029/2011GL047435>.
- Head, J.W., et al., 2001. Geological processes and evolution. *Space Sci. Rev.* 96, 263–292.
- Heap, M.J., Byrne, P.K., Mikhail, S., 2017. Low surface gravitational acceleration of Mars results in a thick and weak lithosphere: implications for topography, volcanism, and hydrology. *Icarus* 281, 103–114.
- Herrero-Gil, A., Egea-González, I., Ruiz, J., Romeo, I., 2019. EStructural modeling of lobate scarps in the NW margin of Argyre impact basin, Mars. *Icarus* 319, 367–380.
- Hofmeister, A.M., 1999. Mantle values of thermal conductivity and the geotherm from phonon lifetimes. *Science* 283, 1699–1706.
- Jaupart, C., Mareschal, J.-C., Iarotsky, L., 2016. Radiogenic heat production in the continental crust. *Lithos* 262, 398–427.
- Kieffer, H.H., et al., 1977. Thermal and albedo mapping of Mars during the Viking primary mission. *J. Geophys. Res.* 82, 4249–4291.
- Kirby, J.F., 2014. Estimation of the effective elastic thickness of the lithosphere using inverse spectral methods: the state of the art. *Tectonophysics* 631, 87–116.
- Kohlstedt, D.L., Mackwell, S.J., 2010. Strength and deformation of planetary lithospheres. In: Watters, T.R., Schultz, R.A. (Eds.), *Planetary Tectonics*. Cambridge University, pp. 397–456.
- Kohlstedt, D.L., Evans, B., Mackwell, S.J., 1995. Strength of the lithosphere: constraints imposed by laboratory experiments. *J. Geophys. Res.* 100 (B9), 17587–17602. <https://doi.org/10.1029/95JB01460>.
- Laskar, J., Levrad, B., Mustard, J.F., 2002. Orbital forcing of the Martian polar layered deposits. *Nature* 419, 375–377.
- Lognonné, P., Banerdt, W.B., Giardini, D., et al., 2019. SEIS: insight’s seismic experiment for internal structure of Mars. *Space Sci. Rev.* 215, 12. <https://doi.org/10.1007/s11214-018-0574-6>.
- McGovern, P.J., Solomon, S.C., Smith, D.E., Zuber, M.T., Simons, M., Wieczorek, M.A., Phillips, R.J., Neumann, G.A., Aharonson, O., Head, J.W., 2002. Localized gravity/topography admittance and correlation spectra on Mars: implications for regional and global evolution. *J. Geophys. Res.* 107, 5136. <https://doi.org/10.1029/2002JE001854> (Corrected in 2004, *J. Geophys. Res.* 109, E07007, doi:10.1029/2004JE002286.).
- McKenzie, D., Jackson, J., Priestley, K., 2005. Thermal structure of oceanic and continental lithosphere. *Earth Planet. Sci. Lett.* 233, 337–349.
- McNutt, M.K., 1984. Lithospheric flexure and thermal anomalies. *J. Geophys. Res.* 89, 11180–11194.
- Meyer, C., 2003. *Mars Meteorite Compendium*. Lyndon B. Johnson Space Cent., NASA, Houston, Tex.
- Morris, R.V., et al., 2016. Silicic volcanism on Mars evidenced by tridymite in high-SiO₂ sedimentary rock at Gale crater. *PNAS* 113 (26), 7071–7076.
- Mueller, K., Vida, A., Robbins, S., Golombek, M., West, C., 2014. Fault and fold growth of the Amathens uplift: implications for late Noachian crustal rheology and heat flow on Mars. *Earth Planet. Sci. Lett.* 408, 100–109.
- Neumann, G.A., et al., 2004. The crustal structure of Mars from gravity and topography. *J. Geophys. Res.* 109, E08002. <https://doi.org/10.1029/2004JE002262>.
- Orosei, R., et al., 2018. Radar evidence of subglacial liquid water on Mars. *Science* 361, 490–493.
- Parro, L.M., et al., 2017. Present-day heat flow model of Mars. *Sci. Rep.* 7, 45629.
- Phillips, R.J., et al., 2008. Mars north polar deposits: stratigraphy, age, and geodynamical response. *Science* 320, 1182–1185.
- Plesa, A.-C., et al., 2016. How large are present-day heat flux variations across the surface of Mars? *J. Geophys. Res. Planets* 121, 2386–2403. <https://doi.org/10.1002/2016JE005126>.
- Plesa, A.-C., Knapmeyer, M., Golombek, M.P., Breuer, D., Grott, M., Kawamura, T., et al., 2018. Present-day Mars’ seismicity predicted from 3-D thermal evolution models of interior dynamics. *Geophys. Res. Lett.* 45, 2580–2589.
- Ranalli, G., 1994. Nonlinear flexure and equivalent mechanical thickness of the lithosphere. *Tectonophysics* 240, 107–114.
- Ranalli, G., 1997. Rheology of the lithosphere in space and time. *Geol. Soc. Spec. Publ.* 121, 19–37.
- Ranalli, G., Adams, M., 2013. Rheological contrast at the continental Moho: effects of composition, temperature, deformation mechanism, and tectonic regime. *Tectonophysics* 609, 480–490.

- Rogers, A.D., Nekvasil, H., 2015. Feldspathic rocks on Mars: compositional constraints from infrared spectroscopy and possible formation mechanisms. *Geophys. Res. Lett.* 42, 2619–2626.
- Ruiz, J., 2014. The early heat loss evolution of Mars and their implications for internal and environmental history. *Sci. Rep.* 4, 4338. <https://doi.org/10.1038/srep04338>.
- Ruiz, J., McGovern, P.J., Tejero, R., 2006a. The early thermal and magnetic state of the cratered highlands of Mars. *Earth Planet. Sci. Lett.* 241, 2–10.
- Ruiz, J., Gómez-Ortiz, D., Tejero, R., 2006b. Effective elastic thicknesses of the lithosphere in the Central Iberian Peninsula from heat flow: implications for the rheology of the continental lithospheric mantle. *J. Geodyn.* 41, 500–509.
- Ruiz, J., et al., 2008. Ancient heat flow, crustal thickness, and lithospheric mantle rheology in the Amenthes region. *Mars. Earth Planet. Sci. Lett.* 270, 1–12.
- Ruiz, J., et al., 2009. Ancient heat flows and crustal thickness at Warrego rise, Thaumasia highlands, Mars: implications for a stratified crust. *Icarus* 207, 631–637.
- Ruiz, J., López, V., Dohm, J.M., 2010. The present-day thermal state of Mars. *Icarus* 207, 631–637.
- Ruiz, J., et al., 2011. The thermal evolution of Mars as constrained by paleo-heat flows. *Icarus* 215, 508–517.
- Sautter, V., et al., 2015. In situ evidence for continental crust on early Mars. *Nat. Geosci.* 8, 605–609.
- Schultz, R.A., Watters, T.R., 2001. Forward mechanical modeling of the Amenthes Rupes thrust fault on Mars. *Geophys. Res. Lett.* 28, 4659–4662.
- Senthil Kumar, P., et al., 2019. Recent seismicity in Valles Marineris, Mars: insights from young faults, landslides, boulder falls and possible mud volcanoes. *Earth Planet. Sci. Lett.* 505, 51–64.
- Solomon, S.C., Head, J.W., 1990. Heterogeneities in the thickness of the elastic lithosphere of Mars: constraints on heat flow and internal dynamics. *J. Geophys. Res.* 95, 11073–11083.
- Sori, M.M., Bramson, A.M., 2019. Water on Mars, with a grain of salt: local heat anomalies are required for basal melting of ice at the south pole today. *Geophys. Res. Lett.* 46, 1222–1231.
- Spohn, T., Grott, M., Smrekar, S.E., et al., 2018. The heat flow and physical properties package (HP3) for the InSight mission. *Space Sci. Rev.* 214, 96. <https://doi.org/10.1007/s11214-018-0531-4>.
- Tasaka, M., Zimmerman, M.E., Kohlstedt, D.L., 2015. Creep behavior of Fe-bearing olivine under hydrous conditions. *J. Geophys. Res. Solid Earth* 120, 6039–6057. <https://doi.org/10.1002/2015JB012096>.
- Taylor, G.J., et al., 2006. Bulk composition and early differentiation of Mars. *J. Geophys. Res.* 111, E03S10. <https://doi.org/10.1029/2005JE002645> (Printed 112 (E3), 2007).
- Taylor, S.R., McLennan, S.M., 2009. *Planetary Crusts: Their Composition, Origin and Evolution*. Cambridge Univ. Press, Cambridge.
- Tesauro, M., et al., 2007. 3D strength and gravity anomalies of the European lithosphere. *Earth Planet. Sci. Lett.* 263, 56–73.
- Thiriet, M., Michaut, C., Breuer, D., Plesa, A.-C., 2018. Hemispheric dichotomy in lithosphere thickness on Mars caused by differences in crustal structure and composition. *J. Geophys. Res.* 123, 823–848.
- Turcotte, D., Schubert, G., 2014. *Geodynamics*, 3rd edition. Cambridge University Press, Cambridge. (636 pp).
- Wade, J., Dyck, B., Palin, R.M., Moore, J.D.P., Smye, A.J., 2017. The divergent fates of primitive hydroospheric water on earth and Mars. *Nature* 552, 391–394.
- Watters, T.R., Schultz, R.A., 2010. *Planetary Tectonics*. Cambridge University Press, Cambridge (531 pp).
- Watts, A.B., 2001. *Isostasy and Flexure of the Lithosphere*. Cambridge Univ. Press, Cambridge (458 pp).
- Watts, A.B., Burov, E.B., 2003. Lithospheric strength and its relation to the elastic and seismogenic layer thickness. *Earth Planet. Sci. Lett.* 213, 113–131.
- Wessel, P., et al., 2013. Generic mapping tools: improved version released. *Eos. Trans. AGU* 94, 409–410.
- Wieczorek, M.A., 2008. Constraints on the composition of the Martian south polar cap from gravity and topography. *Icarus* 196, 506–517.
- Wieczorek, M.A., 2015. Gravity and topography of the terrestrial planets. In: Schubert, G. (Ed.), *Treatise on Geophysics*, 2nd ed. Elsevier, Oxford, pp. 153–193.
- Wieczorek, M.A., Meschede, M., 2018. SHTools — tools for working with spherical harmonics. *Geochem. Geophys. Geosyst.* 19, 2574–2592.
- Wieczorek, M.A., Phillips, R.J., 1998. Potential anomalies on a sphere: applications to the thickness of the lunar crust. *J. Geophys. Res.* 103, 1715–1724.
- Wieczorek, M.A., Zuber, M.T., 2004. Thickness of the Martian crust: improved constraints from geoid-to-topography ratios. *J. Geophys. Res.* 109 (E01009). doi: 10.1029/2003JE0 02153.
- Withers, A.C., Hirschmann, M.M., Tenner, T.J., 2011. The effect of Fe on olivine H₂O storage capacity: consequences for H₂O in the Martian mantle. *Am. Mineral.* 96, 1039–1053.
- Wray, J.J., et al., 2013. Prolonged magmatic activity on Mars inferred from the detection of felsic rocks. *Nat. Geosci.* 6, 1013–1017.
- Zhao, Y.-H., Ginsberg, S.B., Kohlstedt, D.L., 2004. Solubility of hydrogen in olivine: dependence on temperature and iron content. *Contrib. Mineral. Petrol.* 147, 155–161.
- Zhao, Y.-H., Zimmerman, M.E., Kohlstedt, D.L., 2009. Effect of iron content on the creep behavior of olivine: 1. Anhydrous conditions. *Earth Planet. Sci. Lett.* 287, 229–240.
- Zhao, Y.-H., Zimmerman, M.E., Kohlstedt, D.L., 2018. Effect of iron content on the creep behavior of olivine: 2. Hydrous conditions. *Phys. Earth Planet. Inter.* 278, 26–33.
- Zuber, M.T., et al., 2000. Internal structure and early thermal evolution of Mars from Mars Global Surveyor. *Science* 287, 1788–1793.